Deterioration of the oxygen storage and release properties of CeZrO$_4$ by incorporation of calcium

M. López Granados [*], A. Gurbani, R. Mariscal, J.L.G. Fierro

Instituto de Catálisis y Petroleoquímica (CSIC), Marie Curie 2, Campus de Cantoblanco, 28049 Madrid, Spain

ABSTRACT

Calcium was added to CeZrO$_4$ mixed oxide by wet impregnation with a Ca nitrate solution to achieve solids with nominal Ca/(Ce + Zr) atomic ratios of 0.01, 0.02, 0.05, 0.1, 0.2, and 0.5. The solids were calcined at 873 K to decompose the Ca nitrate to CaO. The determination of oxygen storage capacity complete (OSCC) and FTIR studies of the formation of surface superoxide radicals (O$_2^-$) were conducted to study the oxygen storage and release (OSR) properties of the solids. Both measurements indicate that the OSR properties clearly deteriorated for samples with nominal Ca/(Ce + Zr) at. ratios >0.01 (0.9 atoms of Ca nm^{-2}). The degree of deactivation increased with increasing Ca loading; for the sample with the largest Ca loading, the OSCC was ca. 3-fold lower than that of bare CeZrO$_4$. The solids also were characterized by TGA, chemical analysis by TXRF, XRD, N$_2$ isotherms, and XPS. The results indicate that the Ca remained on the surface of the CeZrO$_4$ as supported CaO; the formation of large bulky crystals of CeZrCa mixed oxides by solid-state reaction between the Ca phase and the CeZrO$_4$ did not occur. For Ca loading below the amount required to completely cover the surface (which, experimentally, is ca. 18 atoms of Ca per nm^2 of surface), CaO existed as very well-dispersed CaO domains few atoms thick. Above this value, the surface was completely covered by CaO, and three-dimensional crystals of CaO were formed. Given these results, we propose that the main mechanism for the deterioration of OSR properties of CeZrO$_4$ by incorporation of CaO on the surface by impregnation is fouling: CaO physically prevents contact between the O$_2$ gas and the surface sites of the CeZrO$_4$. It also is likely that a very limited solid-state reaction occurs between the latter two phases, with a CaZrO$_3$-like amorphous oxide formed at the grain boundaries. The formation of this amorphous oxide also can chemically contribute to the deactivation. The relevance of these results in the understanding of the deactivation of TWC by Ca is discussed.

© 2008 Elsevier Inc. All rights reserved.

1. Introduction

The installation of three-way catalysts (TWCs) in exhaust pipes has become the automotive industry's adopted approach to comply with legislation concerning the emission of the most toxic components of gasoline-fueled passenger cars. TWCs considerably reduce the emissions of NO$_x$, unburned hydrocarbons, and CO [1–6]. Although legislation forces manufacturers to guarantee the efficiency of these converters, which have demonstrated their robustness under the tough conditions to which they are subjected, TWCs inevitably deteriorate. TWC deactivation is an important research topic as environmental legislation is becoming more stringent [7–15]. The durability of TWCs must be extended if the increasingly low acceptable emission levels are to be achieved throughout a TWC's lifetime. Understanding the deactivation mechanisms is essential to achieving more durable catalyst cartridges and deploying regeneration procedures to reverse the causes of deactivation [16–20].

Fundamental mechanisms of TWC deactivation have been classified as mechanical, physical fouling, thermal, and chemical [21,22]. Attrition, mechanical breakage, and thermal shock (mechanical) are all irreversible. The fouling by deposits of carbonaceous residues can be reversed by calcination at relatively mild temperatures [23,24]. TWC deactivation by thermal effects involves the sintering of active components, resulting in a loss of surface area of the active components, which in principle is detrimental to catalyst activity. The impact of thermal sintering on TWC efficiency has been minimized through the stabilization of Ce oxide by the addition of Zr (through the formation of solid solutions), however [14,25–28]. Deactivation by chemical mechanisms seems to contribute to a greater extent.

Contaminating elements are deposited on the TWC under working conditions. P, Ca, and Zn, derived from lubricant oil additives (antiwear and detergent additives), are known to be the most con-

centrated contaminants [12,29–32], iron deposits arise from metallic engine parts. The role of these contaminants in the deactivation of TWC is not yet fully understood. Although fouling by physical blockage of catalyst pore structure, due to the formation of an impermeable glassy Zn phosphate and an amorphous glaze-like Ca phosphate (which is more difficult to reverse), has been described for vehicle-aged TWCs [12,33], other aspects remain unexplained.

Current research is aimed at understanding the deterioration of the multiple functions of TWC driven by the presence of these contaminants. Challenges include exploring the sophisticated formulation of the real TWCs, the complex kinetics of the reaction network causing the elimination of gas pollutants, the low concentration of deposited contaminants, and the amorphous character of new phases formed between the contaminants and the components of the TWC and/or between contaminants themselves. Additional complications arise from the complex way in which the contaminants are deposited, as they contact the hot surface as aerosol particles in exhaust gases. The composition of the aerosol particles is complex, including such elements as Ca, P, Zn, and Fe. For the sake of clarity, research can focus on model systems in which the catalyst formulation is simpler and contaminants are incorporated on a case-by-case basis. Following this approach, considerable effort has been devoted to gaining insight into the deactivation mechanism of P and Fe [8,34–37]; other contaminants, such as Ca and Zn, have received much less attention.

Concerning the effect of Ca, research has been done on systems in which Ca is incorporated within the framework of the Ce and/or CeZr oxides using such methodologies as coprecipitation, sol–gel, and microemulsions, which ensure intimate contact between Ca and all of the Ce–Zr cations in the preparation of the precursors [38–41]. These methods, although appropriate for the formation of Ce–Zr–Ca mixed oxides, are not well suited for studying the deactivation of a TWC by Ca. Under real conditions, Ca is deposited initially onto the surface of the TWC and is in contact only with the Ce and Zr cations present on the surface of the solid. Ca compounds are transported in the gas exhaust, are deposited on and react with the hot surface of the catalyst. In principle, this situation differs greatly from the research done so far, in which Ca cations are forced to remain in contact with all of the Ce and Zr cations.

The present work investigated modification of the textural, structural, surface, and OSR properties of $CeZrO_4$ by incorporating only Ca on the surface. The Ce–Zr–Ca solids were then studied to determine whether Ca cations migrated to the bulk of the solid to become part of the framework of the CeZr mixed oxides or remained at the surface of the solid, as well as whether the OSR properties were improved or diminished.

Calcium does not exist alone in the exhaust gas. Moreover, it does not have to be CaO; it can be originally deposited as CaO, $CaCO_3$, $Ca(OH)_2$, Ca phosphates, Ca, Zn phosphates, or another phase. This work focused on the effect of the deposition of CaO; therefore, the research reported in this paper provides a first step toward a better understanding of a much more complex phenomenon. CaO incorporation was achieved by decomposition of the Ca nitrate precursor previously deposited by wetness impregnation of the support with a calcium nitrate solution. This methodology is intended to simulate the actual mode of incorporation: deposition of aerosol particles. It is assumed that the interaction between the CaO deriving from the decomposition of the precursor and the support is similar to that occurring when Ca aerosol particles contact the hot surface; in both cases, the CaO contacts the surface at high temperatures. The impregnation methodology allows for easy reproducibility of the experiment and the setting up of key variables, mainly calcium concentration and calcination temperature, which are very important for quantifying the effect of calcium.

2. Experimental

2.1. Synthesis of Ca-containing solids

A given amount of $Ca(NO_3)_2 \cdot 4H_2O$ (SigmaUltra >99.0%, Sigma–Aldrich) was dissolved in water and then added to a flask containing commercial $CeZrO_4$ (Sigma–Aldrich Cerium Zirconium Oxide 99.0% nanopowder) so as to yield the selected atomic Ca/(Ce + Zr) ratios (ranging from 0.01 to 0.50). The suspension was stirred for 1 h, after which the excess water was removed in a rotary evaporator (323 K, $P < 0.1$ atm). The Ca-containing precursors were then calcined in air at 873 K for 6 h (at a heating rate of 5 K/min) and were designated as CeZrCa, followed by the nominal atomic ratio of Ca/(Ce + Zr) (e.g., CeZrCa 0.01 for a sample with Ca/(Ce + Zr) nominal at. ratio of 0.01).

2.2. Chemical analysis and bulk characterization of the CeZrCa solids

2.2.1. Thermogravimetric analysis

Thermogravimetric analyses (TGA) of the decomposition of the precursors (sample after impregnation but before calcination) were carried out using a Mettler Toledo TGA/SDTA 851^e analyzer. The samples were heated from room temperature up to 1373 K at 5 K min^{-1}, using 250 ml (STP) min^{-1} of synthetic air (20% O_2/N_2).

2.2.2. X-ray diffraction

Powder X-ray diffraction (XRD) was recorded in a 20°–80° 2Θ range in scan mode (0.02°, 1 s) using a Seiffert 3000 XRD diffractometer equipped with a PW goniometer with Bragg–Brentano $\theta/2\theta$ geometry, an automatic split, a bent graphite monochromator, and a Cu anode. The unit cell parameters were obtained by refining the peak positions of the XRD patterns with a least squares refinement method using the CELREF program (CELREF unit-cell refinement software for Windows by Laugier and Bochu; http://www.ccp14.ac.uk/tutorial/lmgp/celref.htm). To determine the width and the position of the peaks, the peak profiles were fitted with the commercially available ANALYZE program (pseudo-Voigt function). The microstrain that can be created by the incorporation of Ca (a divalent cation) within the framework of the $CeZrO_4$ was estimated by the Williamson–Hall method [42]. The microstrain within the crystal structure of $CeZrO_4$ may arise from the presence of O vacancies and/or interstitial Ca^{2+}, from nonhomogeneous values of the planar distance created by nonhomogeneous distribution of Ca^{2+}, etc. The Williamson–Hall method is based on the assumption that the peak width (B_r) is the result of two contributions, the size of the crystal ($B_{crystalline} = k\lambda/L \cos \Theta$) and the size of the microstrain ($B_{strain} = \eta \tan \Theta$), where k is a constant (k values between 0.9 and 1 are generally accepted), λ is the wavelength of the X-ray source, L is the average crystal size, and η is a measurement of the strain in the lattice. The representation of $B_r \cos \Theta$ vs $\sin \Theta$,

$$B_r \cos \Theta = \frac{k\lambda}{L} + \eta \sin \Theta, \tag{1}$$

gives a straight line that intercepts the ordinate axis at $k\lambda/L$ and has a slope of η (a magnitude related to the microstrain).

2.3. Textural and surface characterization of the CeZrCa solids

2.3.1. N_2 adsorption–desorption isotherms

Nitrogen adsorption isotherms were recorded at liquid nitrogen temperature of 77 K using a Micromeritics ASAP 2000 system by incrementally increasing the N_2 dosing pressure up to a relative pressure of $P/P_0 = 1$. Once the adsorption branch was completed, the desorption isotherm was recorded by incrementally decreasing the N_2 relative pressure, P/P_0. Samples were degassed at 413 K for 12 h before the isotherms were recorded.

2.3.2. X-ray photoelectron spectroscopy

X-ray photoelectron spectroscopy (XPS) spectra were recorded with a VG ESCALAB 200R spectrometer equipped with a Mg$K\alpha$ (1253.6 eV) X-ray source and a hemispherical electron analyzer working under constant pass energy mode. The sample was first placed in a copper holder mounted on a sample rod in the pre-treatment chamber of the spectrometer and then outgassed at room temperature for 1 h before being transferred to the analysis chamber. A certain region of the XP spectrum was then scanned a number of times to obtain a good signal-to-noise ratio. The binding energies (BEs) were referenced to the O 1s peak (at 529.1 eV) aris-ing from the O framework of CeZrO$_4$. The appropriateness of this reference selection is based on the consistency of the BEs of the other elements analyzed, as we discuss later when presenting the XPS results. The areas of the peaks were computed by fitting the experimental spectra to Gaussian/Lorenztian curves after removal of the background (Shirley function).

2.4. Oxygen storage and release properties of the CeZrCa solids

2.4.1. Oxygen storage capacity complete measurements

The oxygen storage capacity complete (OSCC; µmol O/g$_{cat}$) was measured at a given temperature by switching the gas flow circu-lating through the solid bed from an inert gas to an O$_2$-containing gas. Before switching, the sample was subjected to pretreatment aimed at removing the contaminants (e.g., carbonates, hydroxides, water) from the surface of the sample and generating oxygen va-cancies by a reduction step. The experiment was conducted as follows. First, a 100-mg sample was loaded into a U-shaped reactor and calcined at 873 K (5 K min^{-1}) in 5% O$_2$/Ar (100 ml min^{-1}) for 1 h. After flushing with Ar to remove any trace of O$_2$ before intro-ducing H$_2$, the sample was reduced in 10% H$_2$/Ar (100 ml min^{-1}) for 1 h at 873 K. Then the feed was switched to an Ar-only flow until no signal from H$_2$ was detected ($m/z = 2$). The feed was then switched to a flow of 1% O$_2$/Ar (100 ml min^{-1}) while the temper-ature was maintained at 873 K. If the solid were storing O$_2$, then the step signal of O$_2$ would be delayed with respect to that of another solid that did not uptake O$_2$. The composition of the gas coming out of the reactor was determined using a BALTZER Prisma QMS 200 mass spectrometer. The amount of O$_2$ stored by the solid was calculated by subtracting the delayed step signal of the solid from a blank experiment with an empty reactor. The experimental error of the measurements was estimated to be within 5%.

2.4.2. Study of the formation of O$_2^-$ radicals by FTIR

IR spectra were recorded with a Nicolet 5700 spectrometer, equipped with a Globar source and a Hg–Te–Cd type cryodetector; the spectra was the average of 256 scans at 4 cm^{-1} resolution, plotted in the absorbance mode. The samples were pressed into self-supporting wafers (ca. 10 mg cm^{-2}), placed in a sample holder, and pretreated in an IR cell designed to work under both vacuum and dynamic conditions. The samples were calcined in room air at 873 K (at a heating rate of 10 K min^{-1}) for 1 h and then outgassed at 873 K for 1 h. Then 100 Torr (1 Torr = 133.3 N m^{-2}) of pure O$_2$ was added to the cell while the wafer was kept at 873 K for 30 min. The cell was then degassed while being cooled to 673 K. At 673 K, 2 Torr of H$_2$ was added, and the temperature increased again to 873 K (10 K min^{-1}) for 15 min. After this, the sample was degassed for 30 min ($P < 5 \times 10^{-4}$ Torr) and then cooled down to room temperature. Finally, the sample was exposed to 20 Torr of O$_2$, and the spectra were recorded. The IR spectra shown here were obtained after subtracting the solid sample background spec-trum obtained under vacuum from the recorded spectrum after O$_2$ chemisorption.
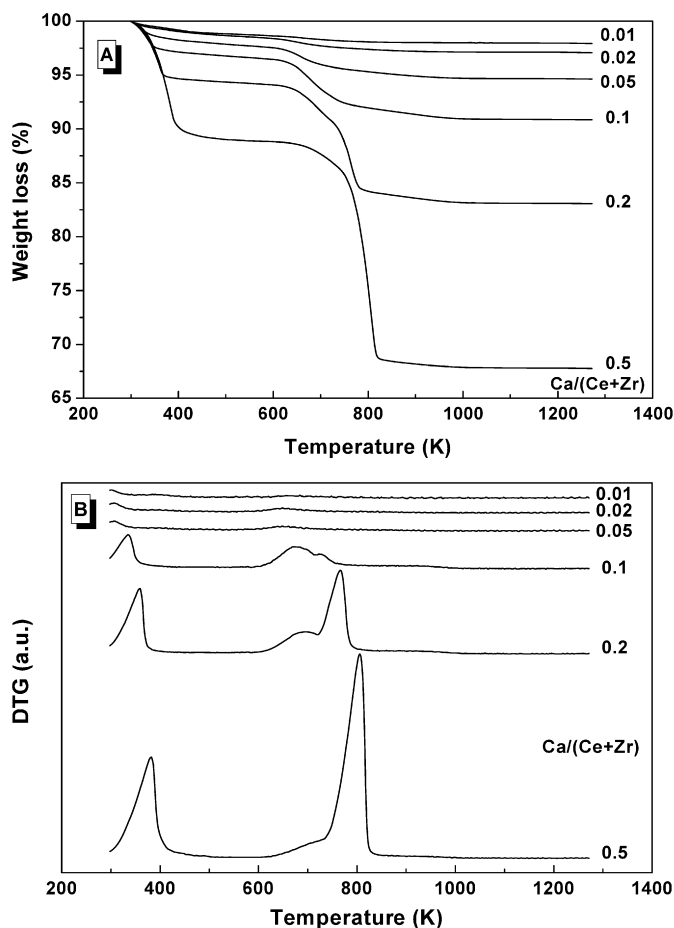

Fig. 1. (A) TGA of the precursors of the CeZrCa solids (samples after impregnation but not calcined) and (B) the derivative curves of the corresponding TGA profiles. (Numbers at the right side correspond to the nominal Ca/(Ce + Zr) atomic ratio.)

3. Results

3.1. Decomposition of the precursors

Fig. 1A shows the TGA results for the uncalcined CeZrCa pre-cursors. For the sake of clarity, the derivative of the TGA curve (DTG), which shows the finer features of the decomposition pro-cesses, is given in Fig. 1B. Two decomposition processes can be observed, one at lower temperatures (from room temperature to 500 K) and a more intense one at higher temperature (600–873 K). The first process was assigned to the evolution of water, which was confirmed by parallel experiments carried out by mass spec-troscopy analysis of the evolution of gases from the sample. Water could arise either from the dehydration of weakly adsorbed H$_2$O on CeZrO$_4$ or from the decomposition of the Ca nitrate tetrahy-drate. The second weight loss process at higher temperatures cor-responds to the evolution of NO and O$_2$ (as observed by mass spectrometry) and thus was assigned to the decomposition of the nitrate groups. In both processes, the weight loss became more in-tense and shifted to higher temperatures with increasing Ca load-ing. According to the derivative curve, two processes could be dif-ferentiated in the "nitrate" decomposition peak at larger Ca load-ings, suggesting the possible presence of two different Ca nitrate species on the surface of the CeZrO$_4$. It is very likely that after calcination, two different species of Ca compound were formed. It must also be stressed that no weight loss was observed beyond 873 K, the calcination temperature of the solids studied in this work.

Table 1
Chemical analysis and textural properties of the CaCeZr samples

Sample	Nominal Ca/(Ce + Zr) at. ratio	TGA Ca/(Ce + Zr) at. ratio	Ca added/$O_{surface}$	S_{BET} $(m^2 g^{-1})$	Mean pore diameter (nm)
CeZrO$_4$	0	–	–	45.2	28
CaCeZr0.01	0.01	0.01	0.06	45.1	27
CaCeZr0.02	0.02	0.03	0.20	44.7	26
CaCeZr0.05	0.05	0.05	0.34	40.4	28
CaCeZr0.1	0.10	0.10	0.66	35.5	26
CaCeZr0.2	0.20	0.22	1.46	29.5	25
CaCeZr0.5	0.50	0.54	3.58	23.1	24
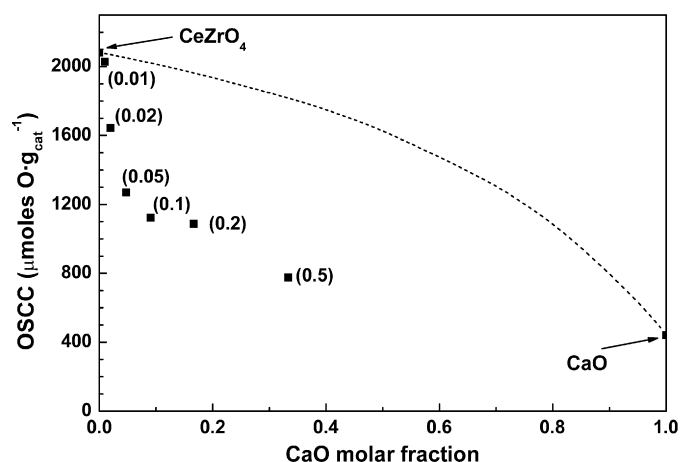
Fig. 2. OSCC of the different samples at 873 K conducted under the switching mode as a function of the CaO molar fraction. Values between brackets correspond to the nominal Ca/(Ce + Zr) at. ratio. (See text for the definition of the dashed line.)

3.2. Chemical analysis

The TGA curves also were used to estimate the Ca/(Ce + Zr) at. ratio by assuming that the weight process occurring between 500 and 873 K corresponded to the decomposition of nitrate groups to NO + O$_2$ and a stoichiometric factor of 2 for the NO$_3$/Ca weight ratio. The values thus obtained, summarized in Table 1, were very similar to the expected nominal values, i.e. (those derived from the amounts of CeZrO$_4$ and Ca nitrate used in the preparation). The values obtained by other analytical techniques (e.g., total reflection X-ray fluorescence) were similar to those obtained by TGA.

On the basis of the chemical composition deduced from TGA, we compared the number of atoms of Ca added in relation to the atoms of oxygen present at the surface layer. The latter parameter was estimated based on the fact that CeZrO$_4$ contains 13.7 superficial oxygen atoms per nm^2 of CeZrO$_4$ [43]. Table 1 gives the values (see the Ca/O$_{surface}$ column) that can be used to evaluate whether or not the surface was overcrowded by Ca, assuming an atomic dispersion of Ca over the CeZrO$_4$ surface. When this ratio is 1, a monolayer of CaO is theoretically formed; when this ratio is >1, the surface is overcrowded, and thus several layers of CaO are expected. We must stress that this result can hold only if Ca is deposited over the entire surface of the solid. We show later that this was not the case here and only the external surface is involved for supporting the Ca phase. Nevertheless, this estimation still provided useful information.

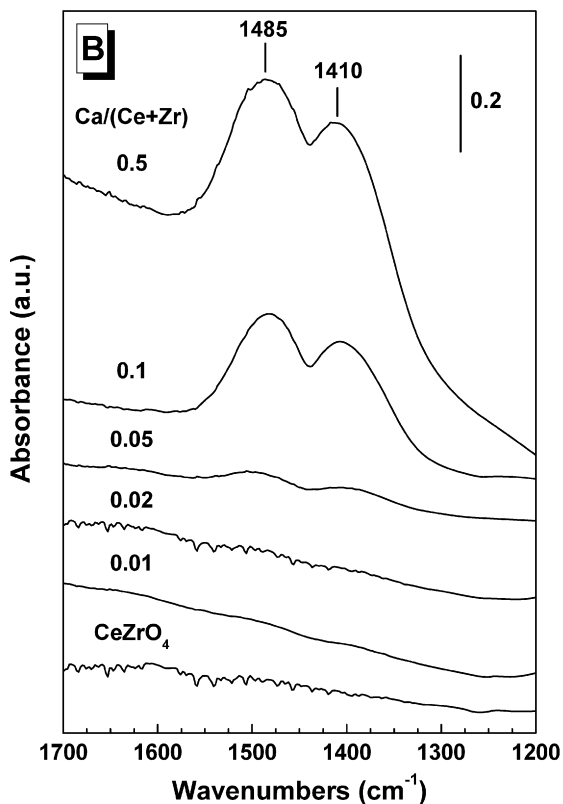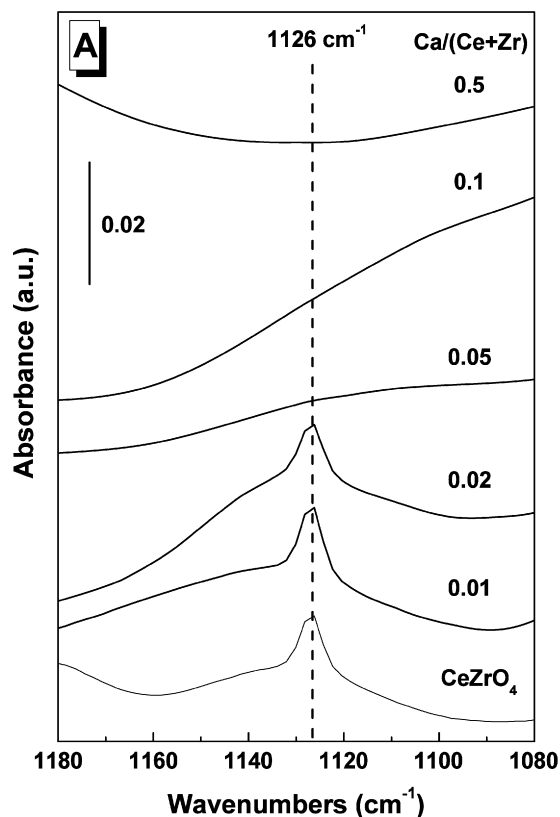### 3.3. Oxygen storage and release properties

Fig. 2 shows the OSCC values (full symbols) of the different samples as a function of the CaO molar fraction. The values in brackets correspond to the nominal Ca/(Ce + Zr) at. ratio. The measurements were conducted at 873 K by switching from an Ar flow

to a 5% O$_2$/Ar flow. The samples were previously subjected to a reduction treatment under a 10% H$_2$/Ar flow at 873 K, to create the O vacancies required for oxygen uptake on both the CeZrO$_4$ and the CaO surfaces [44,45]. The dashed line represents the values that would be expected had no interaction occurred between the phases; in that case, the solids would behave like physical mixtures of CeZrO$_4$ and CaO, and the OSCC would be a linear combination of the OSCC of pure compounds (2081 and 442 μmol O/g$_{cat}$, respectively, with the latter figure corresponding to the experimental values obtained in this work). If this were the case, then the CaO would have a dilution effect on the OSCC of CeZrO$_4$; much smaller (ca. 5-fold lower) O vacancies can be created in the CaO compared with the CeZrO$_4$. What actually occurred was that the incorporation of Ca caused a different pattern, and the OSCC was much more diminished than what was expected for a linear combination of the OSCC properties of the pure phases. A clear deterioration of the OSCC was seen for the samples with nominal Ca/(Ce + Zr) at. ratio >0.01. In terms of Ca atoms per nm^2 of support, the deterioration was important for samples with more than 0.9 at. Ca nm^{-2}. The decrease was 40% for the CeZrCa0.05 sample and >50% for samples with a nominal Ca/(Ce + Zr) at. ratio >0.05 (i.e., >9 molar% of CaO). Actually, the values for sample CeZrCa0.5 were ca. 3-fold lower that those of bare CeZrO$_4$. In short, our findings indicate that inhibition of the OSCC due to the incorporation of Ca into CeZrO$_4$ was caused by a different mechanism than the dilution effect.

Fig. 3A shows the IR region in which O$_2^-$ radicals could be detected. It is now widely accepted that oxygen storage begins with activation of the gaseous O$_2$ molecule on O vacancies associated with reduced cerium sites (Ce^{3+}), known as CUS sites, present on the surface of the Ce–Zr mixed oxides [46–48]. Such activation results in the formation of O radicals on exposure of the surface to O$_2$, due to the reduction of O$_2$ and subsequent oxidation of the coordinatively unsaturated Ce^{3+} sites. Among the various O radicals that can be progressively formed, the superoxide species (O$_2^-$, the first of the series that includes other radicals, such as peroxide [O$_2^{2-}$] and oxide [O$^-$]) is very stable and is considered a key species or an initiator of the oxygen storage process whether the process involves surface or bulk storage phenomena [46–48]. O$_2^-$ radicals can be detected by various techniques, including FTIR [38,46,47,49], which is the technique used in this work. This is another approach to investigating deterioration of the OSR properties and evaluating whether the problem is related to the capacity of O$_2$ activation instead of the other steps of the oxygen storage process, such as surface and bulk O diffusion, vacancy diffusion, and others.

The band at 1126 cm^{-1} observed for the CeZrO$_4$ oxide is assigned to superoxide species. This band also was seen in the CeZrCa0.01 sample. For the CeZrCa0.02 solid, the intensity of the band seemed to decrease. This band was not detected for samples with a Ca/(Ce + Zr) at. ratio >0.02, indicating significant inhibition of the formation of superoxide radicals in those samples. This result is in agreement with those presented in Fig. 2 showing a decreased OSCC for those samples. Fig. 3B shows the region in which carbonate vibrations can be observed. Two strong bands at 1410 and 1485 cm^{-1} are clearly visible in the CeZrCa0.5 sample; these are assigned to the O$_I$–C–O$_I$ asymmetrical and symmetrical stretching vibrations, respectively, of unidentate carbonates present at the surface of CaO [50,51]. XRD revealed the presence of CaO crystals in this sample (see the XRD results in Section 3.4); thus, these bands can be assigned to carbonate groups on the CaO surface. These bands also were clearly visible in the CeZrCa0.2 and CeZrCa0.1 samples; the former spectrum is not shown for the sake of clarity. The weaker incipient bands in the CeZrCa0.05 sample indicate that the CaO phase also must be present in this sample, although XRD did not provide evidence of this. (As we explain later, this is very likely due to the high dispersion and small crys-

Fig. 3. FT-IR spectra regions of the samples where O_2^- radicals (A) and carbonate groups (B) are visible. (The number at the right and left side of the figures indicates the nominal Ca/(Ce + Zr) at. ratio.)
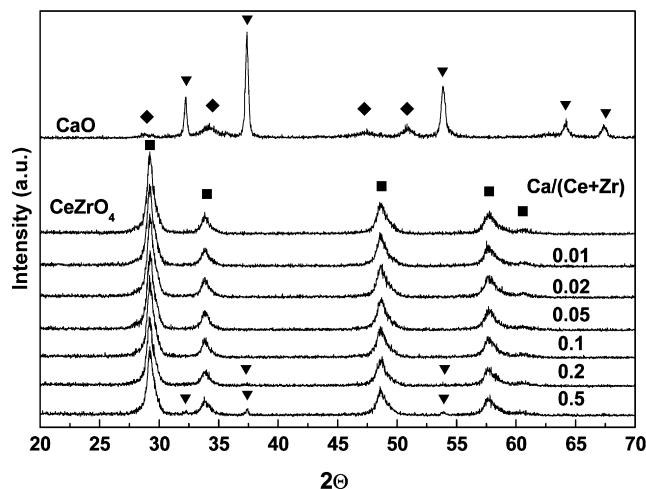
Fig. 4. XRD patterns of the CeZrO$_4$ and CeZrCa samples (for the sake of comparison the pattern of CaO is also included). Number at the right side corresponds to the nominal Ca/(Ce + Zr) at. ratio. (■) CeZrO$_4$, (▼) CaO, (◆) Ca(OH)$_2$.

also exists that the Ca oxide present in the latter samples was of a different nature than that found in the former samples. The salient feature of Fig. 3B is that when carbonate bands are detected, O_2^- radical bands are absent in Fig. 3A. We explore this point in more detail in the next section.

3.4. Bulk and surface characterization

The XRD patterns of the samples are shown in Fig. 4. The features of the CeZrO$_4$ sample (denoted as ■) were as expected for a mixed oxide. The same reflections predominated in the patterns of the samples containing Ca. Small peaks (denoted as ▼) were clearly visible in the CeZrCa0.5 sample. The XRD pattern of commercial CaO (Aldrich, 99.9%) clearly demonstrated that those weak features must be assigned to CaO. The pattern of commercial CaO also showed weaker reflections from Ca(OH)$_2$ (◆ symbols) as the CaO was rapidly hydrated on contact with room air. Incipient peaks from CaO also were seen in the CeZrCa0.2 sample but not in the other Ca samples with lower loading, indicating that a nominal Ca/(Ce + Zr) atomic ratio $\geqslant 0.2$ (surface concentration 18.1 at. Ca nm^{-2}) is required for detection of CaO reflections.

In principle, the nondetection of CaO peaks in the CeZrCa samples with a Ca/(Ce + Zr) at. ratio < 0.2 can be proposed to result from the presence of small and/or ill-crystallized supported CaO particles. But the weak intensity of the CaO peaks also can arise from the lower atomic scattering factor (i.e., lower atomic number) of Ca compared with Ce–Zr. In fact, a sample prepared by physically mixing CaO and CeO$_2$ (Aldrich, CeO$_2$ nanopowder) to obtain a Ca/Ce atomic ratio of 0.5 displayed an XRD pattern (not shown in the figure) with a CaO reflection intensity of the same order as that found in the CeZrCa0.5 solid. In other words, the lower intensity of the reflection of CaO also can be related to the lower atomic scattering factor [42], not necessarily to the presence of a well-dispersed CaO phase. Additional characterization was carried out to explore the hypothesis of the presence of small, very poorly crystallized CaO particles, because the XRD results did not provide sufficient support for this hypothesis.

The XRD investigation also was directed at determining whether Ca cations were located within the framework of the Ce–Zr mixed oxide by partial substitution of the Ce^{4+} or Zr^{4+} cations by Ca^{2+}—in other words, whether a Ce–Zr–Ca mixed oxide was formed rather than a Ca oxide dispersed over the surface. To do this, the cell parameter was estimated by applying the CELREF software to the main peaks assigned to the CeZrO$_4$ phase (denoted as ■). If

tal size of the CaO.) The carbonate bands were not detected in the samples with lower Ca loadings, likely because the concentration of carbonate bands was below the detection limit. The possibility

Table 2
Cell parameter of CeZrCa samples

Sample	a (Å)
CeZrO$_4$	5.3123 ± 0.0074
CeZrCa0.01	5.2941 ± 0.0070
CeZrCa0.02	5.2960 ± 0.0068
CeZrCa0.05	5.2987 ± 0.0112
CeZrCa0.10	5.2965 ± 0.0058
CeZrCa0.20	5.3046 ± 0.0043
CeZrCa0.50	5.3080 ± 0.0058
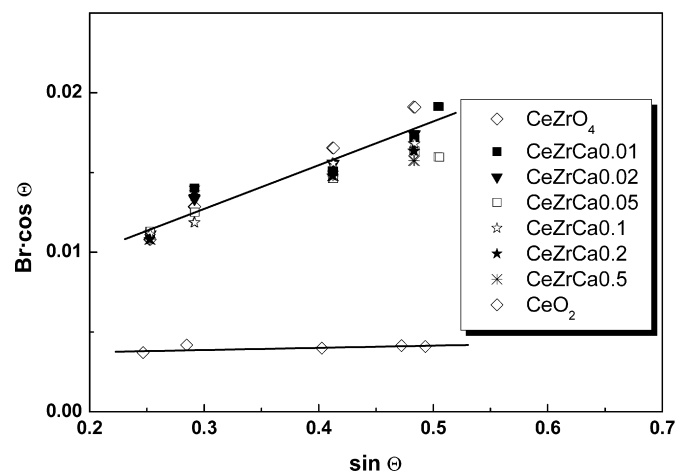
Fig. 5. Williamson–Hall plot for CeZrO$_4$ and CeZrCa samples. CeO$_2$ is also included as a reference.

Fig. 6. N$_2$ adsorption (full symbols) and desorption isotherms (open symbols) of CeZrO$_4$, CeZrCa0.1, CeZrCa0.2, and CeZrCa0.5 samples.

Ca^{2+} were within the framework, then a variation in the cell parameter would be expected. For simplicity, we assumed that the diffraction peaks corresponded to the cubic phase. The a parameter of the different samples are summarized in Table 2. On one hand, the difference in size between the Ca^{2+} cations (1.0 Å for 6-fold coordination and 1.12 for 8-fold coordination) and the Ce^{4+} (0.97 Å for 8-fold coordination) or Zr^{4+} (0.84 Å for 8-fold coordination) cations [52] should be reflected in a slight expansion of the cell parameter. But on the other hand, to achieve charge neutrality, O vacancies must be created, which would result in the opposite effect: decreasing cell parameters. It has been found [39] that with the actual formation of Ce–Zr–Ca mixed oxide, the latter effect prevails, and contraction of the cell parameter is observed. Based on the data of Table 2, and taking into account the relative error of the measurements, we cannot conclude that our samples demonstrated a variation in the cell parameters and thus cannot conclude that a Ce–Zr–Ca mixed oxide was formed.

Other evidence of the presence of Ca^{2+} cations within the CeZrO$_4$ oxide framework can come from the detection of a structural microstrain. The presence of a microstrain can serve as proof of the formation of CeZrCa mixed oxides, which was not obtained from analysis of the cell parameters. The Williamson–Hall (W–H) plot method has been applied [42] to the different samples to estimate the strains; the results are shown in Fig. 5. (Note than only the reflections displayed in Fig. 4 are represented in Fig. 5: the large width and low intensity of the peaks at larger diffraction angles preclude accurate determination of their width and thus their inclusion in the W–H plot.) For comparison, the results for CeO$_2$ (Aldrich CeO$_2$ nanopowder) also are included. Clearly, the slope and intercept of the W–H straight line of the CeZrCa samples differed greatly from those of CeO$_2$ nanopowder, as did the particle size and microstrain; however, the divergences between the points of the different CeZrCa samples are not very intense, and they are below the experimental error of the technique. In other words, the points of the different CeZrCa samples can be fitted to straight lines of similar slope and intercept, because the Ca-containing samples have a microstrain similar to that found in CeZrO$_4$. Therefore, the W–H analysis also suggests that incorporation of Ca in the CeZrO$_4$ sample did not result in the formation of a Ce–Zr–Ca mixed oxide. If the Ca is not inside the framework, then it must be located over the CeZrO$_4$ surface; in other words, XRD provides indirect evidence that Ca oxide was located over the surface of the support.
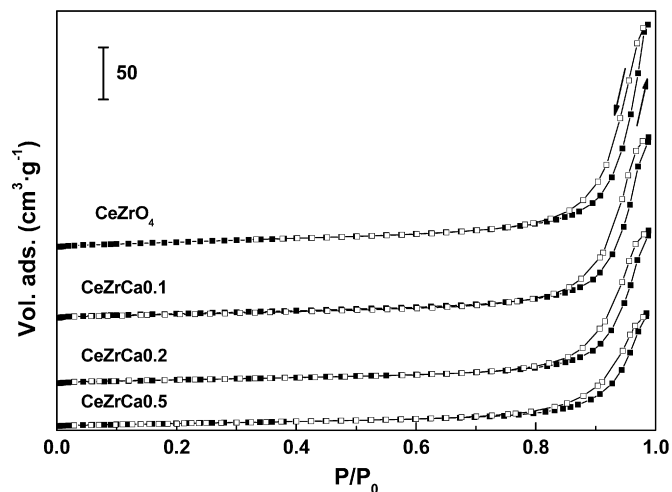
Fig. 6 shows the N$_2$ adsorption–desorption isotherms of the CeZrO$_4$ sample and of the samples with Ca/(Ce + Zr) at. ratios of 0.1, 0.2, and 0.5. The isotherms of the samples with lower atomic ratios were undistinguishable from that of the CeZrO$_4$ solid, and thus they are not included in the figure. The isotherms are shifted vertically to provide a clearer view. The isotherms correspond to type IV with a type H1 hysteresis loop, indicating that the isotherms arose from the agglomeration of oxide particles, resulting in the formation of large interparticle mesopores both at the external surface and in the inner region of the agglomerate. Table 1 gives the values for the specific area calculated according to the BET method and the mean pore size estimated from the desorption branch of the isotherm by the BJH method. It can be seen that the specific area decreased with increasing Ca content; the value for the CeZrCa0.5 was half that of the CeZrO$_4$. In contrast, the mean pore size did not change much, and the mean pore size of the CeZrCa0.5 sample was quite similar to that of the CeZrO$_4$ sample (only 14% smaller). This finding suggests that the addition of Ca resulted in the formation of a Ca phase deposited only on the external surface of the agglomerates. The more external pores were filled, but without modification of those still available in the inner core of the agglomerate. The final result is that the specific surface area decreased because fewer pores were available for adsorption, but the mean pore size of the remaining inner pores was not altered. To explain this finding, we must take into account that the impregnating solution readily filled the external pores. As the solution penetrated further, high pressure was generated, as the air trapped in the inner pores was pushed by the front line of the solution, preventing the complete filling of the pores. Some previous calculations have estimated that pressures as high as tens of bar can be generated [53].

Fig. 7 shows the photoelectron spectra of the Ce 3d, Zr 3d, Ca 2p, and O 1s core levels for the different samples. The Ce 3d core level was dominated by the contributions from Ce^{4+} cations. The presence of three spin-orbit doublets (designated V, V'', V''', U, U'', and U''' following the notation of Burroughs [54]) and their positions are representative of Ce^{4+} [8,35]. On the other hand, the
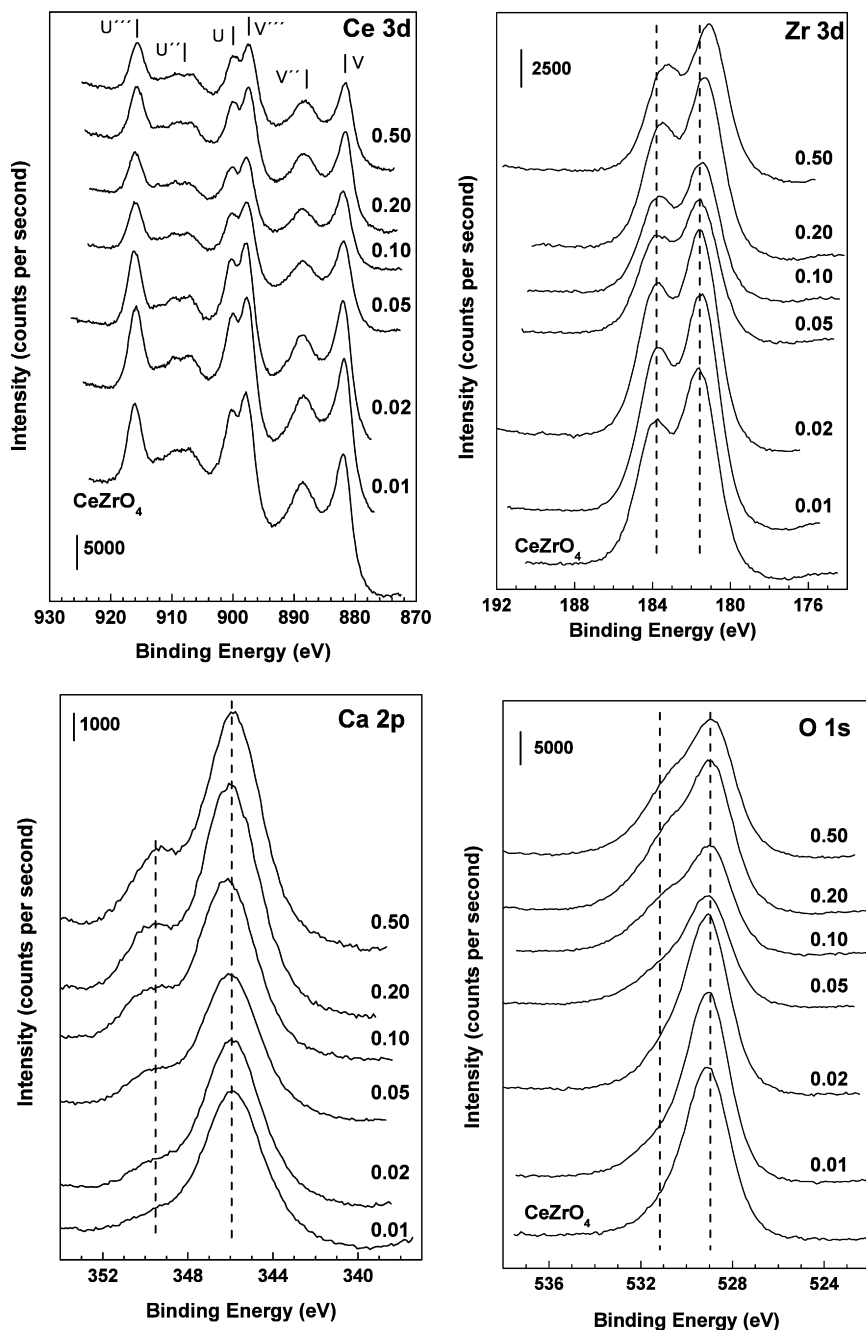
Fig. 7. XPS spectra of the main electronic levels of CeZrCa (number at the right side of the figures indicates the nominal Ca/(Ce + Zr) at. ratio).

presence of Ce^{3+} can be semiqualitatively estimated based on two features of the spectrum. The first of these features is the well-defined valley between the V and V'' peaks. The Ce^{3+} core level displayed four peaks, one located in the valley; therefore, the better defined the valley, the smaller the amount of Ce^{3+} present [8,35]. The second feature is the intensity of the U''' peak. The Ce^{3+} cation displays no features at this position; therefore, the greater the intensity of the peak V''', the smaller the concentration of Ce^{3+}. Both of the foregoing features indicate that although the presence of small amounts of Ce^{3+} cannot be disregarded, Ce^{4+} predominated on the surfaces of all samples. This also means that the addition of Ca^{2+} did not result in a noticeable increase in Ce^{3+} concentration, and that CUS sites (O vacancies and Ce^{3+} sites) were not formed. Therefore, XPS provided additional evidence that Ca^{2+} was not incorporated within the framework of $CeZrO_4$. It also must be stressed that no change was observed in the position of

the Ce 3d peaks of the Ca-containing samples with respect to those of the $CeZrO_4$ sample. This suggests that Ca and Ce may not have been interacting (i.e., a mixed oxide was not formed); however, this is not a definitive conclusion, because the formation of a Ca and Ce interaction and the shift of the Ce 3d peak position are not necessarily related, and the possibility of formation of a Ce–Ca mixed oxide cannot be completely discounted.

In contrast, a shift to a lower BE of the Zr $3d_{5/2}$ (∼181.5 eV) and Zr $3d_{3/2}$ (∼184.0 eV) core levels was clearly observed in the samples with a nominal Ca/(Ce + Zr) atomic ratio >0.1. This indicates an interaction between Ca and Zr. The formation of a Zr–Ca mixed oxide can be proposed. Actually, in CeZrCa0.2 and CeZrCa0.5 samples calcined at 1273 K, XRD revealed the presence of $CaZrO_3$ (results not shown). A small incipient shift was observed in the CeZrCa0.1 sample, but this was not seen in the samples with a Ca/(Ce + Zr) at. ratio <0.1. Consequently, it seems reasonable to

conclude that incorporation of Ca in $CeZrO_4$ by impregnation resulted in the formation of a Zr–Ca mixed oxide (very likely $CaZrO_3$) as a consequence of the solid-state reaction between $CeZrO_4$ and CaO microcrystals. This means that Zr^{4+} cations were being extracted from the $CeZrO_4$ phase, forming Zr-poorer Ce–Zr mixed oxides. The finding does not contradict the XRD results, because it does not mean that an extensive reaction occurred, only that some interfacial reaction, restricted to very superficial regions, occurred. XRD could not detect the $CaZrO_3$ phase because of its amorphous character.

In the spectrum for the Ca 2p core level shown in Fig. 7, the Ca $2p_{1/2}$ and Ca $2p_{3/2}$ doublet should have been seen with a separation of 3.5 eV and an intensity ratio of 1/2 [55]. The latter condition clearly was not fulfilled. The Zr $3p_{1/2}$ component of the Zr 3p doublet was located at ca. 346.0 eV, overlapping the Ca $2p_{3/2}$ peak. The Zr $3p_{1/2}$ core level predominated in this XPS region for the samples with lower Ca concentration. Although the intensity of the Ca 2p contributions must grow as the Ca becomes more concentrated, the Ca $2p_{1/2}$ peak is the only contribution of a Ca 2p peak that can be easily quantified without interference from the contribution of Zr $3p_{1/2}$. That is why this peak was selected for Ca quantification purposes. On the other hand, no change was observed in the position of the Ca $2p_{1/2}$ peak even though $CaZrO_3$ could be formed. It may be that Ca 2p levels were insensitive to the Ca–Zr interaction detected at the Zr 3d level.

Fig. 7 also depicts the O 1s core level. The O 1s peak of $CeZrO_4$ was dominated by the peak at ~529.1 eV, which is assigned to the framework O^{2-}. A weak shoulder at ca. 531.1 eV also was visible; this can be assigned to hydroxyl and/or to carbonate groups present on the surface of the CeZr mixed oxide [56]. With increasing Ca concentration, the peak at ca. 531.1 eV became more intense. This can be explained by the presence of hydroxyl or carbonate groups at the surface of the CaO microcrystals [55]; the greater the CaO concentration, the larger the contribution to this peak. (The possible presence of an O 1s contribution from the O^{2-} of CaO cannot be discarded; its position is close to that of Ce oxides (529.1 eV), and thus the two can be confused).

The XPS experimental results can be compared with those obtained using the Kerkhof–Moulijn (KM) model [57–61]. The KM model estimates the intensity ratio between two elements, one element present in a supported phase that is deposited over a support that contains the other element and with large specific surface. The KM model considers the catalyst to comprise sheets of support with cubic crystallites with dimension c deposited onto the support. The thickness (t) of the support slabs are estimated from the density (ρ_s) and the specific surface (S) of the support ($t = 2S/\rho_s$). The model assumes that the electrons leave the sample in a perpendicular direction to the surface. The relation between the intensity of the supported element and the element from the support is given by Eq. (2) (following the Kerkhof–Moulijn notation)

$$\left[\frac{I_p}{I_s}\right]_{KM} = \left[\frac{p}{s}\right]_b \left[\frac{D(\varepsilon_p)}{D(\varepsilon_s)}\right]\left[\frac{\sigma_p}{\sigma_s}\right]\left[\frac{\beta_1}{2}\right]\left[\frac{1+e^{-\beta_1}}{1-e^{-\beta_2}}\right]\left[\frac{1-e^{-\alpha}}{\alpha}\right]. \quad (2)$$

Here the subscript s represents the support phase and the subscript p represents the supported phase; in the original work of Kherkof et al. [57], the supported phase was called the promoter phase. We kept the same nomenclature for the sake of clarity. The dimensionless support thicknesses, β_1 and β_2, are defined as t/λ_{ss} and t/λ_{ps}, where λ_{ss} and λ_{ps} are the inelastic mean free path (IMFP) of the photoelectron from s passing through the support (ss) or through the supported phase (ps). The dimensionless crystallite size α is defined as c/λ_{pp}, where λ_{pp} is the IMFP of the photoelectron from p passing through the supported phase (pp). In this case, p refers to parameters from the Ca $2p_{1/2}$ core level and s refers to parameters from the Ce 3d core level. The ratio

$(p/s)_b$ is the $(Ca/Ce)_b$ bulk atomic ratio, σ is the cross-section of the photoelectrons, and $D(\varepsilon)$ is the detector efficiency for the different photoelectrons. We use the parameters from the Ca $2p_{1/2}$ core level, because the contribution of Ca $2p_{3/2}$ is overshadowed by the strong Zr $3p_{1/2}$ core level.

A particular case of this model is when the supported phase is very well dispersed either atomically or forming monolayer-like domains with monoatomic thickness onto the supporting phase. In such a simplified situation, the intensities ratio between the two elements (KMm, where m stands for monolayer) is given by the equation

$$\left[\frac{I_p}{I_s}\right]_{KMm} = \left[\frac{p}{s}\right]_b \left[\frac{D(\varepsilon_p)}{D(\varepsilon_s)}\right]\left[\frac{\sigma_p}{\sigma_s}\right]\left[\frac{\beta_1}{2}\right]\left[\frac{1+e^{-\beta_1}}{1-e^{-\beta_2}}\right]. \quad (3)$$

The ratio of Eq. (3) to Eq. (2) is the factor $(1-e^{\alpha})/\alpha$, the value of which (between 0 and 1) depends on the average crystal size, c. This factor is 1 for monoatomic dispersion and tends to 0 as the dispersion decreases, because large metallic crystals are formed. Taking this into account, when comparing the values deduced from Eq. (3) with the experimental values, three situations can occur. If Eq. (3) gives values reasonably similar to experimental XPS I_{Ca2p}/I_{Ce3d} ratios, it is because the supported fraction is very well dispersed [58,59]. If the experimental XPS values are smaller than those obtained from the simpler Eq. (3), it is because the Ca phase is deposited as microcrystals with average size c and are not well dispersed. It also may be possible that the experimental ratio is larger than values deduced from Eq. (2). In such a situation, it has been proposed that the supported phase concentrates at the external surface of the support [58]. In our case, this would mean that only the external pores of $CeZrO_4$ solid are covered by the well-dispersed Ca phase, whereas the inner pores remain uncovered.

The $\sigma_{Ca2p_{1/2}}$ and σ_{Ce3d} values of 1.74 and 48.24, respectively, were those tabulated by Scofield [62]. $(Ca/Ce)_b$ can be determined from the chemical analysis and by assuming a Ce/Zr at. ratio of 1. β_1 is defined by the expression $2/\rho_s S\lambda_{Ce3d}$ and β_2 is defined by $2/\rho_s S\lambda_{Ca2p}$, where ρ_s is the bulk density of $CeZrO_4$ phase (6.6 g cm^{-3}), S is the specific surface of the bare support (45.2 m^2 g^{-1}), and λ_{Ce3d} (0.9 nm) and λ_{Ca2p} (1.7 nm) are the inelastic mean free paths (IMFPs) of the Ce 3d and Ca $2p_{1/2}$ photoelectrons passing through the $CeZrO_4$ phase. These IMFPs were estimated using the model of Cumpson et al. [63]. When comparing the specific surface of $CeZrO_4$ (45.2 m^2 g^{-1}) with another support with lower molecular weight, such as carbon or SiO_2, it must be noted that carbon with 1100 m^2 g^{-1} and SiO_2 with 221 m^2 g^{-1} have the same surface per mol of support as the $CeZrO_4$ used in the present work. It also is assumed that the $D(\varepsilon_p)/D(\varepsilon_s)$ can be estimated from the kinetic energy (E_{kin}) of the Ca $2p_{1/2}$ and Ce 3d photoelectrons according to the expression $E_{kin\,Ce\,3d}/E_{kin\,Ca\,2p}$ since in the case of an XPS spectrophotometer with a hemispherical analyzer working under constant pass energy mode, the detector efficiency can be considered proportional to the inverse of the E_{KIN} of the photoelectron [57].

Table 3 summarizes the intensity ratios of some of the more representative photoelectrons of the elements present in the samples (O 1s, Ca $2p_{1/2}$, and Ce 3d). The table also compares the experimental intensity ratios between Ca $2p_{1/2}$ and Ce 3d with those obtained from the simplified KM model developed in Eq. (3). For the KMm values, it is assumed that the specific surface area of the support did not change with the Ca incorporation, in other words, that there was no interaction between the CaO and the $CeZrO_4$ and that the Ca phase was deposited onto the $CeZrO_4$ support. Although the specific surface area of the entire solid decreased, the surface of the support was not modified.

The first comment in Table 3 refers to the XPS intensity ratio of O 1s and Ce 3d photoelectrons. As the nominal Ca concentration grew, this ratio decreased. Thus, the ratio for the CeZrCa0.5 sample,

Table 3
Ca/Ce and O/Ce atomic ratios determined from the XPS results and Ca/Ce atomic ratios estimated by the Kerkhof–Moulijn monolayer model

Samples	Exp. XPS $I_{O\,1s}/I_{Ce\,3d}$	Exp. XPS $I_{Ca\,2p}/I_{Ce\,3d}$[a]	KMm $I_{Ca\,2p}/I_{Ce\,3d}$[a]
CeZrO$_4$	5.89	–	–
CeZrCa0.01	5.85	0.003	0.001
CeZrCa0.02	5.44	0.005	0.003
CeZrCa0.05	4.55	0.011	0.005
CeZrCa0.10	3.41	0.023	0.01
CeZrCa0.20	3.28	0.022	0.023
CeZrCa0.50	3.15	0.033	0.056

[a] Intensity ratios of Ca $2p_{1/2}$ and Ce 3d photoelectrons.

3.15, was almost half that of the CeZrO$_4$ sample, 5.89. This is a first indication of the presence of increasingly larger amounts of Ca phase at the surface of the solid that shields the Ce photoelectrons.

Comparing the experimental XPS $I_{Ca\,2p}/I_{Ce\,3d}$ ratio with those obtained from Eq. (3) (KM monolayer model) is also of interest, because it can provide information about whether or not the Ca phase is being deposited, forming monolayer-like deposits, and also whether microcrystals of the Ca phase are present. Both of these values are summarized in Table 3.

Experimental XPS $I_{Ca\,2p}/I_{Ce\,3d}$ ratios of all of the samples were substantially larger than the KMm values deduced from Eq. (3), except for the CaCeZr0.2 and CaCeZr0.5 samples, in which the XPS ratios are similar to and smaller than the XPS ratios, respectively. That the experimental XPS $I_{Ca\,2p}/I_{Ce\,3d}$ values for the CeZrCa 0.01, 0.02, 0.05, and 0.1 samples were larger than the Eq. (3) KMm ratios suggests that the Ca phase was deposited only at the external surface pores [58], in agreement with the N$_2$ isotherm results. The inner pores were not filled. Unfortunately, XPS cannot be used to detect CaO monolayer-like domains at the surface; we discuss this possibility later. The fact that the experimental XPS ratio of the CeZrCa0.5 sample was smaller than the KMm is consistent with the detection of large CaO crystals in this sample by XRD; when crystals of the promoter phase (Ca phase) are present at the surface of the support, the XPS $I_{Ca\,2p}/I_{Ce\,3d}$ ratio must be smaller than those calculated from Eq. (3) [57,58]. The CeZrCa0.2 sample is in an intermediate case, because incipient CaO crystals were detected by XRD.

4. Discussion

Our characterization results are compatible with the model summarized in Scheme 1. The particles of CeZrO$_4$ are agglomerated into larger particles, and external and internal mesopores are

created. For the sake of simplicity, spherical particles are assumed for CeZrO$_4$, but different and irregular shaped particles are more realistic. Scheme 1 is a two-dimensional representation of CeZrO$_4$ particles, but the actual situation is a three-dimensional arrangement. The Ca phase does not react extensively with the CeZrO$_4$, and bulk CeZrCa mixed oxide is not formed. Ca remains at the external surface of the agglomerate of particles of CeZr mixed oxide. If any formation of mixed oxides between Ca and CeZr occurs, it is restricted to the interface between the Ca phase and CeZrO$_4$.

We also propose that the Ca phase is in the form of well-dispersed CaO domains over the surface of the CeZrO$_4$. When the amount of Ca that is incorporated is larger than the amount required to totally cover the surface (a value will be provided below), three-dimensional crystals are formed.

All of the experimental results presented in this work can be explained by this hypothesis, which is basically a description of the system after incorporation of Ca by impregnation and when the solids are subjected to calcination temperatures $\leqslant$873 K. Any model in which a significant fraction of the Ca cations migrate to the inner bulk of the CeZrO$_4$ oxide, forming CeZrCa mixed oxides, would contradict any of the characterization results presented here.

N$_2$ isotherms are in harmony with the model. Interparticle pores in the inner region of the agglomerates are not filled with Ca phase and remain practically unaffected; only the external surface pores are filled with CaO. The KMm model applied to the XPS results also is in agreement with the model presented in Scheme 1.

A comparison of the amount of Ca atoms incorporated and the amount of oxygen present on the surface of the solid (see the "Ca added/O$_{surface}$" column in Table 1) suggests that well-dispersed CaO patches are a few atoms thick. Thus, if we assume that CaO monolayer-like domains are formed, then, theoretically, the monolayer is achieved when Ca surface concentration is equal to the amount of O on the CeZrO$_4$ surface, that is, 13.7 Ca nm^{-2}. A simple calculation indicates that this should occur at a bulk Ca/(Ce + Zr) at. ratio of 0.15. For higher Ca loadings, large three-dimensional CaO crystals then should start to appear. This estimation assumes that Ca can be deposited over the entire surface, but this is not the case; actually, only the external surface is covered, and the inner pores are not filled. Consequently, it must be assumed that monolayer formation should occur at a Ca loading somewhat below 13.7 Ca nm^{-2}. The characterization results do indicate that the change from well-dispersed CaO domains to large three-dimensional crystals occurs at a higher Ca concentration. Incipient CaO crystals are detected by XRD in the CeZrCa0.2 sample,
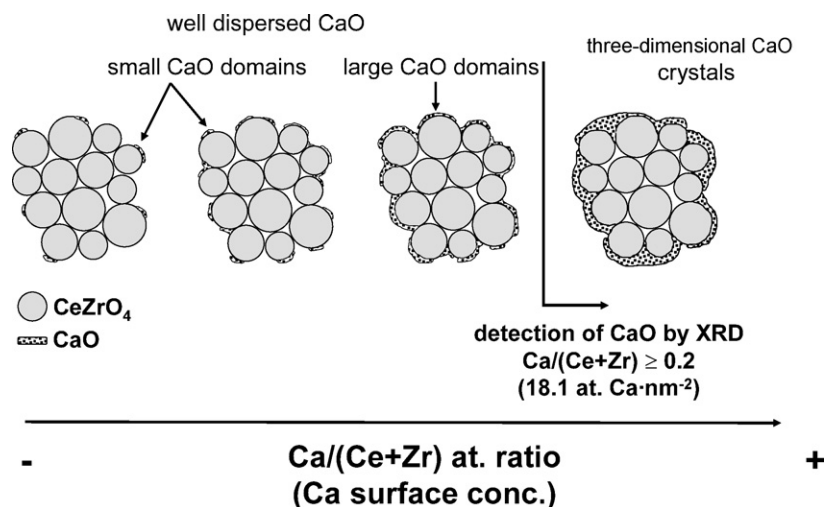
Scheme 1. Simplified representation of the deposition of CaO onto the external surface of the aggregates of CeZrO$_4$ as larger amounts of CaO are incorporated.

which corresponds to 18.1 Ca nm^{-2}. All of these estimations suggest that below this experimental amount (i.e., that required to cover the external surface), deposition of well-dispersed CaO is forming patches of CaO a few atoms thick, not CaO monolayer-like domains. These CaO patches must be a maximum of two or three atoms thick.

TGA detected two different types of Ca species deposited on the CeZrO$_4$. It can be proposed that the lower-temperature peak of the nitrate decomposition arises from the decomposition of well-dispersed Ca nitrate species that predominate at lower Ca loading, and that the higher-temperature peak present in CeZrCa0.2 and CeZrCa0.5 samples arises from larger Ca nitrate microcrystals. The shift toward higher temperatures can be explained according to the same hypothesis. Therefore, the TGA results support the idea that two different CaO species—supposedly well-dispersed CaO domains and large three-dimensional CaO crystals—are formed after calcination of the latter Ca nitrate species.

The incorporation of Ca to CeZrO$_4$ causes a deterioration of its OSR properties at a Ca/(Ce + Zr) at. ratio >0.01; below this ratio, the deactivation is negligible. These results apparently contradict those for other CeZrCa systems in which the Ca is incorporated into CeZr mixed oxide through microemulsion or coprecipitation methods. But it must be taken into account that in those methods, Ca is incorporated during formation of the precursor of the CeZr mixed oxide. This ensures that Ca is in intimate contact with the Ce and Zr cations from the very start of the mixed-oxide formation [38–41]. The Ca occupies framework sites within the CeZr mixed-oxide structure, and all of the Ca cations are in close proximity to Ce and Zr cations. As a result, a high concentration of O vacancies is present in these systems, and their OSC properties should be improved. In our case, however, the Ca was incorporated by impregnation and the CeZrCa mixed oxide was not formed, and so the OSR behavior followed a different pattern.

CaO deteriorates the OSR properties of CeZrO$_4$ by surface fouling irrespective of the type of CaO oxide present on the surface (highly dispersed or large crystals). The CaO covers the surface and prevents contact between the chemisorption sites at the CeZrO$_4$ surface and the O$_2$ gas. When the CaO is deposited as well-dispersed CaO patches, the greater the CaO concentration, the smaller the fraction of CeZrO$_4$ left exposed and the more significant the deterioration of OSR properties. For samples with very high Ca concentrations, large three-dimensional CaO crystals are formed on the previously fully covered CeZrO$_4$ surface. The OSR properties are then mainly defined by those of CaO. The fact that the presence of carbonate bands coincides with the lack of detection of O$_2^-$ bands reinforces this model; the CeZrO$_4$ surface is extensively covered by large CaO crystals, and no superoxide radicals can be observed by FTIR. (O$_2^-$ radicals cannot be detected in CaO.)

Because of the impregnation methodology used in this work, the inner pores remain unfilled. This does not necessarily occur in automotive catalysts. Ca compounds contact the surface as aerosol particles carried in the gas phase, and thus resistance to this penetration would not be expected. A different methodology, such as chemical vapor deposition or chemical grafting of suitable compounds, may produce complete covering of the outer and inner pores; however, this more complex methodology would yield conclusions similar to those reached in the present study. The only expected difference would concern the limit value of Ca surface concentration that defines the transition from highly dispersed CaO to large three-dimensional CaO crystals; higher values would be required.

The possibility of formation of a ZrCa mixed oxide in the impregnated samples cannot be disregarded; it is highly likely that an amorphous CaZrO$_3$-like oxide is present in some of the CaO particle–CeZrO$_4$ particle interfaces. This can result from the solid-

state reaction between the former phases, but this reaction is very limited and it is not a bulk phenomenon. The formation of a Zr–Ca mixed oxide, like ZrCaO$_3$, exerts a negative effect on the OSR by causing a withdrawal of Zr from the CeZrO$_4$ and the formation of nanodomains in which the Ce–Zr mixed oxide has Zr/Ce at. ratio <1. The OSR of Zr-poorer Ce–Zr mixed oxides is worse than that of CeZrO$_4$ [47,48].

Our findings may be of interest when assessing the deactivation of a commercial TWC by Ca aged under actual driving conditions. Under such conditions, Ca compounds present in the exhaust gas as aerosol particles reach the hot surface of the catalyst. Thus, our results suggest that a TWC can be deactivated by Ca contamination through deterioration of the OSR properties of the CeZr mixed oxide. This deactivation can occur only if the amount of Ca is such that a significant fraction of the surface of the CeZr mixed oxide is covered by CaO.

Finally, some aspects must be taken into consideration when considering future investigation into the deactivation of TWCs. First, this work provides a first step toward the understanding of a very complex phenomenon; other contaminants are present in the gas phase and can simultaneously contaminate the washcoat. Second, because a TWC can reach temperatures above 873 K during its life cycle, the investigation must be extended to solids calcined at higher temperatures. Last but not least, other active components (e.g., noble metals, like Pd and Rh, and a γ-Al$_2$O$_3$ support) are present in TWCs. The research on model samples should be continued with further studies using more sophisticated preparation methodology and more complex formulations in which other contaminants besides Ca are added to fully characterize the interactions between the different contaminants (e.g., Ca, P, Zn) and the rest of the TWC components or between the different contaminants themselves.

The present study is likely relevant to the study of another type of automotive catalysts as well: nitrogen oxide storage and release (NSR) catalytic traps. NSR catalysts typically contain Ce or mixed cerium oxides and alkaline earth oxides (Ba and, to a lesser extent, Sr and Mg) deposited on alumina supports. The similar chemistry of Ca and these cations demonstrates that although during preparation the intention is to confine the alkaline earth material to the alumina–support phase, the potential exists for the alkaline earth cations to be transported to the cerium phase during either calcination step or subsequent use in the vehicle. Thus, the deactivation mechanism for the OSR properties of Ce mixed oxides described in this work may be relevant to the NSR systems as well.

5. Conclusions

Based on our findings, we can state the following conclusions:

1. The incorporation of Ca to CeZrO$_4$ by impregnation with a Ca nitrate and further calcination at 873 K resulted in deterioration of the OSR properties of the CeZrO$_4$. The degree of deactivation was low when small amounts of Ca were added (<0.9 Ca nm^{-2}) but increased with increasing Ca loading. This phenomenon was demonstrated by OSCC measurements and by the study of the formation of O$_2^-$ radicals by FTIR.
2. Characterization of the solids suggested that Ca remained on the surface of the CeZrO$_4$ catalyst. When the solid was calcined at 873 K, the formation of CeZrCa mixed oxides by solid state reaction between the Ca phase and the CeZrO$_4$ either did not occur or if it did occur, was limited to the interface between these two phases. Actually, a CaZrO$_3$-like amorphous oxide likely was formed at the grain boundaries. The Ca phase over the support comprised well-dispersed CaO patches of a few atoms in thickness. As CaO loading increased, increasingly larger fractions of the CeZrO$_4$ surface were covered. Once

the amount of Ca required to totally cover the surface was reached, further incorporation of Ca resulted in the formation of large, three-dimensional CaO crystals.

3. The main mechanism in the deterioration of OSR properties involved surface fouling irrespective of the chemical nature of the Ca oxide species. The presence of calcium oxide physically prevented contact between the O_2 gas and the active sites of the $CeZrO_4$. The larger the fraction of $CeZrO_4$ fouled by calcium oxide, the more intense the deterioration of the OSR properties. The formation of a $CaZrO_3$-like phase also would contribute to the OSR deterioration; in that case, the deterioration mechanism would be chemical. $CaZrO_3$ formation gave rise to the withdrawal of Zr cations from the $CeZrO_4$ structure, leaving a Zr-poorer Ce–Zr mixed oxide with worse OSR properties.

4. Our findings also may be relevant for understanding the mechanism of deactivation of a TWC aged under actual conditions, because it has been found that Ca is present in used TWCs.

References

[1] M. Shelef, R.W. McCabe, Catal. Today 62 (2000) 35.
[2] R.J. Farrauto, R.M. Heck, Catal. Today 51 (1999) 351.
[3] R.M. Heck, R.J. Farrauto, Appl. Catal. A Gen. 221 (2001) 443.
[4] M.V. Twigg, Appl. Catal. B Environ. 70 (2007) 2.
[5] J. Kašpar, P. Fornasiero, N. Hickey, Catal. Today 77 (2003) 419.
[6] H.S. Gandhi, G.W. Graham, R.W. McCabe, J. Catal. 216 (2003) 433.
[7] P.S. Lambrou, A.M. Efstathiou, J. Catal. 240 (2006) 182.
[8] C. Larese, F. Cabello Galisteo, M. López Granados, R. Mariscal, J.L.G. Fierro, P.S. Lambrou, A.M. Efstathiou, J. Catal. 226 (2004) 443.
[9] A.K. Neyestanaki, F. Klingstedt, T. Salmi, D.I. Murzin, Fuel 83 (2004) 395.
[10] M. Moldovan, S. Rauch, G.M. Morrison, M. Gomez, M.A. Palácios, Surf. Interface Anal. 35 (2003) 354.
[11] D.E. Angove, N.W. Cant, Catal. Today 63 (2000) 371.
[12] C. Larese, F. Cabello Galisteo, M. López Granados, R. Mariscal, J.L.G. Fierro, M. Furió, R. Fernández-Ruíz, Appl. Catal. B Environ. 40 (2003) 305.
[13] C. Larese, F. Cabello Galisteo, M. López Granados, R. Mariscal, J.L.G. Fierro, Appl. Catal. B Environ. 48 (2004) 113.
[14] J.R. González-Velasco, J.A. Botas, R. Ferret, M.P. González-Marcos, J.L. Marc, M.A. Gutiérrez-Ortiz, Catal. Today 59 (2000) 395.
[15] L.F. Liotta, A. Longo, A. Macaluso, A. Martorana, G. Pantaleo, A.M. Venezia, G. Deganello, Appl. Catal. B Environ. 48 (2004) 133.
[16] F. Cabello Galisteo, R. Mariscal, M. López Granados, J.L.G. Fierro, P. Brettes, O. Salas, Environ. Sci. Technol. 39 (2005) 3844.
[17] F. Cabello Galisteo, R. Mariscal, M. López Granados, J.L.G. Fierro, R.A. Daley, J.A. Anderson, Appl. Catal. B Environ. 59 (2005) 227.
[18] F. Cabello Galisteo, R. Mariscal, M. López Granados, M.D. Zafra Poves, J.L.G. Fierro, V. Kroger, R.L. Keiski, Appl. Catal. B Environ. 72 (2007) 272.
[19] S.Y. Christou, H. Birgersson, J.L.G. Fierro, A.M. Efstathiou, Environ. Sci. Technol. 40 (2006) 2030.
[20] H. Birgersson, M. Boutonnet, S. Järås, L. Eriksson, Top. Catal. 30–31 (2004) 433.
[21] G.C. Koltsakis, A.M. Stamatelos, Prog. Energy Combust. Sci. 23 (1997) 1.
[22] L.A. Carol, N.E. Newman, G.S. Mann, SAE Techn. Paper Ser. (1989) 892040.
[23] C.H. Bartholomew, Appl. Catal. A Gen. 212 (2001) 17.
[24] T.N. Angelidis, V.G. Papadakis, Appl. Catal. B Environ. 12 (1997) 193.
[25] C. Bozo, F. Gaillard, N. Guilhaume, Appl. Catal. A Gen. 220 (2001) 69.
[26] J. Kašpar, P. Fornasiero, M. Graziani, Catal. Today 50 (1999) 285.
[27] J. Kašpar, P. Fornasiero, J. Solid State Chem. 171 (2003) 19.
[28] J.R. González-Velasco, J.A. Botas, J.A. González-Marcos, M.A. Gutiérrez-Ortiz, Appl. Catal. B Environ. 12 (1997) 61.
[29] T.N. Angelidis, S.A. Sklavounos, Appl. Catal. A Gen. 133 (1995) 121.
[30] D.D. Beck, J.W. Sommers, C.L. DiMaggio, Appl. Catal. B Environ. 11 (1997) 257.
[31] M.J. Rokosz, A.E. Chen, C.K. Lowe-Ma, A.V. Kucherov, D. Benson, M.C.P. Peck, R.W. McCabe, Appl. Catal. B Environ. 33 (2001) 205.
[32] M. López Granados, F. Cabello Galisteo, R. Mariscal, A. Alifanti, A. Gurbani, J.L.G. Fierro, R. Fernández-Ruíz, Appl. Surf. Sci. 252 (2006) 8442.
[33] D.R. Liu, J.S. Park, Appl. Catal. B Environ. 2 (1993) 49.
[34] L. Xu, G. Guo, D. Uy, A.E. O'Neill, W.H. Weber, M.J. Rokosz, R.W. McCabe, Appl. Catal. B Environ. 50 (2004) 113.
[35] C. Larese, M. López Granados, R. Mariscal, J.L.G. Fierro, P.S. Lambrou, A.M. Efstathiou, Appl. Catal. B Environ. 59 (2005) 13.
[36] M. López Granados, F. Cabello Galisteo, P.S. Lambrou, M. Alifanti, R. Mariscal, A. Gurbani, J. Sanz, I. Sobrados, A.M. Efstathiou, J.L.G. Fierro, Top. Catal. 42–43 (2007) 443.
[37] D. Uy, A.E. O'Neill, L. Xu, W.H. Weber, R.W. McCabe, Appl. Catal. B Environ. 41 (2003) 269.
[38] M. Fernández-García, A. Martínez-Arias, A. Guerrero-Ruíz, J.C. Conesa, J. Soria, J. Catal. 211 (2002) 326.
[39] M. Fernández-García, X.Q. Wang, C. Belver, A. Iglesias-Juez, J.C. Hanson, J.A. Rodríguez, Chem. Mat. 17 (2005) 4181.
[40] J.A. Rodríguez, X.Q. Wang, J.C. Hanson, G. Liu, A. Iglesias-Juez, M. Fernández-García, J. Chem. Phys. 119 (2003) 5659.
[41] Y. Zhang, S. Andersson, M. Muhammed, Appl. Catal. B Environ. 6 (1995) 325.
[42] C. Suryanarayana, M. Grant Norton, X-Ray Diffraction: A Practical Approach, Norton Plenum Press, New York, 1998.
[43] Y. Madier, C. Descorme, A.M. Le Govic, D. Duprez, J. Phys. Chem. B 103 (1999) 10999.
[44] R. Di Monte, J. Kašpar, Top. Catal. 28 (2004) 47.
[45] T. Anastasiadou, L.A. Loukatzikou, C.N. Costa, A.M. Efstathiou, J. Phys. Chem. B 109 (2005) 13693.
[46] C. Descorme, Y. Madier, D. Duprez, J. Catal. 196 (2000) 167.
[47] D. Duprez, C. Descorme, T. Birchem, E. Rohart, Top. Catal. 16 (2001) 49.
[48] Catalysis by Ceria and Related Materials, in: A. Trovarelli (Ed.), Catalytic Science Series, vol. 2, Imperial College Press, New York, 2002.
[49] L. Can, K. Domen, K. Maruya, T. Onishi, J. Am. Chem. Soc. 111 (1989) 7683.
[50] A.A. Davydov, M.L. Shepotko, A.A. Budneva, Catal. Today 24 (1995) 225.
[51] P. Kassner, M. Baerns, Appl. Catal. A Gen. 139 (1996) 107.
[52] R.D. Shannon, C.T. Prewitt, Acta Crystallogr. Struct. Sci. B 25 (1969) 925.
[53] G. Ertl, H. Knözinger, J. Weitkamp, Preparation of Solid Catalysts, Wiley–VCH, Weinheim, 1999.
[54] P. Burroughs, A. Hamnett, A.F. Orchard, G. Thornton, J. Chem. Soc. Dalton Trans. 17 (1976) 1686.
[55] M. López Granados, M.D. Zafra Poves, D.M. Alonso, R. Mariscal, F. Cabello Galisteo, R. Moreno-Tost, J. Santamaria, J.L.G. Fierro, Appl. Catal. B Environ. 73 (2007) 317.
[56] A.E. Nelson, K.H. Schulz, Appl. Surf. Sci. 210 (2003) 206.
[57] F.P.J.M. Kerkhof, J.A. Moulijn, J. Phys. Chem. 83 (1979) 1612.
[58] V. Leon, Surf. Sci. 339 (1995) L931–L934.
[59] A.M. Venezia, Catal. Today 77 (4) (2003) 359.
[60] A.M. Venezia, L. Palmisano, M. Schiavello, C. Martin, I. Martin, V. Rives, J. Catal. 147 (1994) 115.
[61] A.M. Venezia, A. Rossi, L.F. Liotta, A. Martorana, G. Deganello, Appl. Catal. A Gen. 147 (1996) 81.
[62] J.H. Scofield, J. Electron. Spectrosc. Relat. Phenom. 8 (1976) 129.
[63] P.J. Cumpson, M.P. Seah, Surf. Interface Anal. 25 (1997) 430.